

Leo I: the classical dwarf spheroidal galaxy with the highest dark-matter density

R. Pascale¹, * C. Nipoti², F. Calura¹, and A. Della Croce^{1,2}

¹ INAF - Osservatorio di Astrofisica e Scienza dello Spazio di Bologna, via Gobetti 93/3, 40129 Bologna, Italy

² Dipartimento di Fisica e Astronomia 'Augusto Righi', Alma Mater Studiorum - Università di Bologna, via Gobetti 93/2, 40129 Bologna, Italy

Received ...; accepted ...

ABSTRACT

Dwarf spheroidal galaxies (dSphs) are known for being strongly dominated by dark matter (DM), which makes them convenient targets for investigating the DM nature and distribution. Recently, renewed interest in the dSph Leo I has resulted from claims suggesting the presence of a central supermassive black hole, with mass estimates that challenge the typical expectations for dSphs, which are generally thought to host intermediate-mass black holes (IMBHs). However, [Pascale et al. \(2024\)](#) presented new upper limits on the black hole mass, which are consistent with the expected range for IMBHs, solving the concerns raised in previous studies. Building on the analysis of [Pascale et al. \(2024\)](#), we examine the DM properties of Leo I inferred from the state-of-the-art dynamical models of that paper. Our results indicate that Leo I is the galaxy with the highest DM density among the classical dSphs, with a central DM density (measured at a distance of 150 pc from the galaxy centre) $\rho_{150} = 35.5^{+3.8}_{-4.7} \times 10^7 M_{\odot} \text{ kpc}^{-3}$. According to our model, the DM density profile has logarithmic slope $\gamma_{150} = -0.89^{+0.21}_{-0.17}$ at 150 pc, in line with literature values. At smaller distances the DM distribution flattens into a core of constant density, with a core radius of $r_c = 72^{+40}_{-32}$ pc. Combined with the small pericentric distance of Leo I's orbit in the Milky Way, the new estimate of ρ_{150} makes Leo I decisive in the study of the anticorrelation between pericentre and central DM density, and suggests that the anticorrelation could be significantly steeper and more pronounced than previously estimated. Finally, despite its DM dominance, Leo I does not emerge as the most favorable target for indirect DM detection: the inferred DM decay D and annihilation J factors, $\log D(0.5^\circ) [\text{GeV cm}^{-2}] = 17.94^{+0.17}_{-0.25}$ and $\log J(0.5^\circ) [\text{GeV}^2 \text{ cm}^{-5}] = 18.13^{+0.17}_{-0.18}$ are consistent with previous estimates and lower than the highest values measured in dSphs.

Key words. galaxies: individual: Leo I - galaxies: dwarf - stars: kinematics and dynamics - - Cosmology: dark matter

1. Introduction

According to the current Λ CDM cosmological model, dwarf galaxies play a crucial role in cosmic structure formation, with hierarchical evolution driven by the merging of smaller systems ([Lacey & Cole 1993, 1994](#)), and dwarf galaxies dominating the galaxy population ([Marzke et al. 1998](#)). As such, dwarf galaxies serve as key probes for cosmology, especially given also the increasing tensions observed at these smaller scales ([Bullock & Boylan-Kolchin 2017; Sales et al. 2022](#)). Among dwarfs, dwarf spheroidal galaxies (dSphs) satellites of the Milky Way (MW) are of particular importance due to their proximity to us and their significant dark matter (DM) content ([Battaglia & Nipoti 2022](#)). These two aspects combined make dSphs important testbeds for cosmological models and excellent sites for studying DM ([Gilmore et al. 2007](#)). As an example, due to the lack of emission in other bands apart from optical, dSphs are ideal targets to look for gamma-ray emission related to DM particles annihilation or decay ([Bonnivard et al. 2015; Geringer-Sameth et al. 2015; Evans et al. 2016; Boddy et al. 2020; Li et al. 2021; Andrade et al. 2024](#)).

Another example of the importance of dSphs in the study of DM is the core-cusp problem ([de Blok 2010; Bullock & Boylan-Kolchin 2017](#)). While DM-only simulations predict that halos should develop cuspy central density profiles, observational studies of low surface brightness and gas-rich dwarf galax-

ies suggest that their DM distributions are shallower, with central cores of constant density. In dSphs, determining the inner DM density is more challenging due to their lack of gas, which leaves only stellar kinematics as tracers of the gravitational potential. As a result, different methods and assumptions in modeling stellar orbits can lead to contrasting conclusions, contributing to the ongoing tension on this scale with some analyses suggesting the presence of cored profiles, others consistent with cuspy distributions ([Walker et al. 2009; Strigari et al. 2008; Amorisco & Evans 2011; Breddels & Helmi 2013; Strigari et al. 2017; Pascale et al. 2018; Read et al. 2019, hereafter R19; Hayashi et al. 2020, hereafter H20; Arroyo-Polonio et al. in prep.](#)). The origin of such cores remains debated, as it may depend on interaction between baryons and DM ([Read & Gilmore 2005; Governato et al. 2012; Nipoti & Binney 2015](#)) or indicate a need for alternative DM models ([Governato et al. 2015; Hui et al. 2017](#)).

Leo I is one of the most luminous and massive dSphs within the MW halo, with a stellar mass of $5.5 \times 10^6 M_{\odot}$ ([McConnachie 2012](#)). It has a regular morphology, with an elliptical structure on the plane of the sky. The ellipticity is $e \equiv 1 - \frac{b}{a} = 0.31 \pm 0.01$ ([Muñoz et al. 2018](#)), with a and b the semi-major and -minor axes, respectively. This value is comparable to that of other well-known dSphs. The heliocentric distance is 256.7 ± 13.3 kpc ([Méndez et al. 2002; Bellazzini et al. 2004; Held et al. 2010; Pacucci et al. 2023](#)), which makes Leo I the most distant dSph currently identified as satellite of the MW. We will adopt $D = 256.7$ kpc throughout this analysis.

* e-mail: raffaele.pascale@inaf.it

The orbit of Leo I is well known, with [Mateo et al. \(2008\)](#) providing a robust estimate of its line-of-sight (l.o.s.) velocity ($v_{\text{los}} \simeq 282 \text{ km s}^{-1}$). [Sohn et al. \(2013\)](#) determined the bulk velocity in proper motion (PM) for the first time, using HST images over a 5-year baseline. The tangential velocity component of the galaxy is significantly large; however, it remains lower than its radial component, resulting in a fairly elliptical orbit. [Sohn et al. \(2013\)](#) showed that Leo I likely entered the MW about 2.33 ± 0.21 Gyr ago, having its first pericentric passage approximately 1.05 ± 0.09 Gyr ago. More recently, [Battaglia et al. \(2022\)](#), using *Gaia* eDR3 data, provided a much more precise estimate of the bulk PM for Leo I, allowing for a more accurate orbital calculation. Their results indicate a very small bulk PM, leading to a more radial orbit with a pericentric passage of $r_{\text{peri}} = 35^{+24}_{-20}$ kpc. This value represents one of the smallest pericentric distances observed among the known dSphs.

For the classical dSphs orbiting the MW an empirical anticorrelation is found between their orbital pericentric radius and their central DM density ρ_{150} , conventionally measured at 150 pc from the center of the dwarf ([Kaplinghat et al. 2019](#); [Cardona-Barrero et al. 2023](#); [Andrade et al. 2024](#)). The physical interpretation of the existence of such anticorrelation is still debated, and it could either find its explanation within CDM models or alternative models of DM, such as self-interacting DM ([Correa et al. 2015](#)). In any case, given its small pericentric radius and being also one of the dSphs with the highest DM central density (e.g. [Hayashi et al. 2020](#); [Andrade et al. 2024](#)), the galaxy is an especially interesting object to study in this context.

Distant galaxies serve as valuable tools for investigating the distribution of DM within the outer halo of the MW, providing essential constraints on the potential of the MW at large distances. However, their analysis requires a cautious approach. For example, the discrepancy between the PM estimates of [Sohn et al. \(2013\)](#) and [Battaglia et al. \(2022\)](#) may lead to different dynamical mass estimates in the outer parts of the MW ([Battaglia et al. 2022](#)). Nonetheless, this impact should remain moderate since the overall velocity of Leo I is primarily influenced by its l.o.s. component. In any case, [Battaglia et al. \(2022\)](#) and [Sohn et al. \(2013\)](#), along with estimates from [Fritz et al. \(2018\)](#) and [Gaia Collaboration et al. \(2018\)](#), agree on the timing of the (only) pericentric passage, $\simeq 1$ Gyr ago.

Leo I underwent an extended star-forming phase, marked by recurring bursts lasting until approximately 1 Gyr ago ([Ruiz-Lara et al. 2021](#)), making it among the youngest MW dSphs ([Bellazzini et al. 2004](#)). Notably, the latest star formation episode (1 Gyr ago) coincides with its closest approach to the MW centre, which supports the hypothesis that ram pressure stripping close to the MW center quenched the star formation, capturing Leo I in the transition from dIrr to dSph ([Ruiz-Lara et al. 2021](#)).

Recently, Leo I has garnered renewed interest due to the possible detection of a supermassive black hole (SMBH) at its center, as reported by [Bustamante-Rosell et al. \(2021\)](#). This SMBH, with a mass intriguingly comparable to the total stellar mass of the system, would challenge established models of black hole (BH) formation and evolution. To reconcile this anomaly, [Pacucci et al. \(2023\)](#) proposed that Leo I was initially more massive, losing a significant portion of its mass due to tidal interactions with the MW, rendering the SMBH consistent with a more massive original system. However, this model is unconvincing due to the unrealistic orbit required and its inconsistency with the mass-metallicity relation. Recently, [Pascale et al. \(2024, hereafter P24\)](#) reanalyzed Leo I, using the same dataset as [Bustamante-Rosell et al. \(2021\)](#) but employing more sophisticated models and a statistically robust approach. This

Table 1: Leo I main structural parameters.

Parameter	Value	Reference
Ra	10h 08m 28.1s	(a)
Dec	+12d 18m 23s	(a)
D [kpc]	256.7 ± 13.3 kpc	(b)
M_V	-12.0 ± 0.3	(a)
$M_\star [M_\odot]$	5.5×10^6	(a)
e	0.31 ± 0.01	(c)
r_c [arcmin]	3.3 ± 0.3	(a)
r_t [arcmin]	12.6 ± 1.5	(a)
R_{eff} [arcmin]	3.65 ± 0.03	(c)

Notes. From top to bottom: Right ascension and Declination (Ra, Dec); Distance D ; V-Band absolute magnitude M_V ; stellar mass M_\star ; ellipticity e ; core radius r_c and truncation radius r_t from one-component King models; effective radius R_{eff} . References: (a) [McConnachie \(2012\)](#); (b): [Pacucci et al. \(2023\)](#); (c): [Muñoz et al. \(2018\)](#); (d): [Irwin & Hatzidimitriou \(1995\)](#)

reanalysis excludes the presence of a SMBH and shows that Leo I's central region could, at most, host an intermediate-mass black hole (IMBH), with an estimated upper limit on the mass $\log M_{\text{BH}} [M_\odot] < 5.27$ at 1σ , thus suggesting that Leo I's internal kinematics is actually consistent with a no-BH scenario.

In this work, we build upon the models presented by [P24](#), shifting our focus toward a detailed analysis of the DM properties in Leo I, as the models presented by [P24](#) also provide accurate predictions for the DM distribution within the galaxy. Specifically, we investigate the inner structure of Leo I's DM halo, aiming to constrain its inner slope. Furthermore, we reassess ρ_{150} , the DM density within 150 pc, and incorporate this revised estimate into the context of established scaling relations. We provide new estimates of the decay and annihilation D and J factors, essential quantities in the search for gamma-ray emission from DM particle interactions.

This paper is organized as follows. In Section 2 we give a brief recap of the dataset and the models used by [P24](#). In Section 3 we discuss our results and compare them with the literature. Section 4 we draw our conclusions.

2. Data and models

In this section, we provide a brief summary of the dataset and the dynamical models used by [P24](#). For an extensive discussion, we refer the reader to [P24](#), and to their appendix A for a comprehensive description of the Bayesian strategy and likelihood methodology adopted, which we do not report here for the sake of conciseness.

2.1. Data

The dataset integrates photometric and kinematic measurements. The photometric component is based on the surface brightness profile from [Bustamante-Rosell et al. \(2021\)](#), derived from SDSS g-band imaging. This profile extends from the central 30 pc to approximately 1.5 kpc. Unlike the profiles adopted in previous studies, the surface brightness profile derived in this work both probes the innermost regions of Leo I and extends to significantly large projected radii. Also, in the central galaxy region,

Table 2: Inference on the models free parameters.

Parameter	Prior	Median	1 σ	3 σ
$\log M_\star [M_\odot]$	[6.439, 7.041]	6.759	[6.567, 6.939]	[6.441, 7.040]
$\log J_{c,\star} [\text{kpc km s}^{-1}]$	[-2, 0]	-0.378	[-0.453, -0.316]	[-0.698, -0.190]
$\log J_\star [\text{kpc km s}^{-1}]$	[0, 1]	0.460	[0.441, 0.479]	[0.401, 0.522]
$\log J_{t,\star}^* [\text{kpc km s}^{-1}]$	-	-	-	-
$h_{z,\star}$	[0, 1.5]	0.783	[0.737, 0.825]	[0.639, 0.929]
$g_{z,\star}$	[0, 1.5]	1.024	[1.008, 1.040]	[0.977, 1.069]
Γ_\star	[0, 3]	1.378	[1.289, 1.461]	[1.040, 1.616]
B_\star	[3, 9]	6.576	[6.336, 6.805]	[5.918, 7.295]
η_\star	[0.5, 10]	7.377	[5.489, 8.979]	[3.315, 9.985]
α_\star (fixed)	-	0	-	-
$\log M_{\text{DM}} [M_\odot]$	[6, 11]	8.846	[8.561, 9.053]	[8.091, 9.422]
$\log J_{c,\text{DM}} [\text{kpc km s}^{-1}]$	[-1.5, 0]	-0.394	[-1.089, 0.320]	[-1.497, 1.128]
$\log J_{\text{DM}} [\text{kpc km s}^{-1}]$	[0, 2.5]	1.707	[1.321, 2.170]	[0.335, 2.494]
$\log J_{t,\text{DM}} [\text{kpc km s}^{-1}]$ (fixed)	-	1.92	-	-
$h_{z,\text{DM}} = g_{z,\text{DM}}$	[0, 1.5]	0.927	[0.557, 1.227]	[0.130, 1.416]
Γ_{DM}	[0, 3]	1.301	[0.974, 1.567]	[0.146, 2.156]
B_{DM}	[3, 10]	5.479	[3.854, 7.803]	[3.011, 9.983]
η_{DM}	[0.5, 5]	2.985	[1.493, 4.310]	[0.522, 4.996]
α_{DM} (fixed)	-	1.93	-	-
$\log M_{\text{BH}} [M_\odot]$	[1, 7]	3.894	[2.105, 5.274]	[1.005, 5.835]
c	[25, 35]	29.773	[29.581, 29.952]	[29.449, 30.063]

Notes. List of free parameters alongside the adopted prior distributions (which are uniform in the reported interval), and the median values, 1 σ and 3 σ confidence intervals of the posterior distributions resulting from the analysis of P24.

* Since $\alpha_\star = 0$, the value of $J_{t,\star}$ is unimportant, see equation (3).

crowding and completeness was assessed using high-resolution HST images. However, it must be stressed that, despite the applied corrections, the use of wide-field, ground-based imaging for a galaxy at such a large heliocentric distance makes the computation of the surface brightness profile prone to potential biases and limitations. In particular, ground-based imaging of distant, low-surface-brightness dwarf galaxies is notoriously challenging due to the extremely low surface brightness of these systems, which often approaches the limiting sky background level.

For the inner galaxy regions, the models fit the central line-of-sight velocity distributions (LOSVDs) obtained from integral field spectroscopy data. These distributions provide dynamical information extending out to approximately 110 pc from the galaxy's center. Finally, beyond 110 pc, the authors used the galaxy's velocity dispersion profile computed from the sample of radial velocities of Leo I's members from Mateo et al. (2008).

2.2. Models

Leo I's models from P24 are based on analytic distribution functions (DFs) depending on the action integrals \mathbf{J} (Binney 2014; Cole & Binney 2017). In their analysis, Leo I is represented as a multi-component galaxy, with DF-based stellar and DM components, and an optional central BH of mass M_{BH} described by a Keplerian, fixed contribution to the total potential

$$\Phi_{\text{tot}}(r) = \Phi_\star(r) + \Phi_{\text{DM}}(r) + \Phi_{\text{BH}}(r), \quad (1)$$

where Φ_\star , Φ_{DM} and Φ_{BH} are the stellar, DM and BH potentials. For stars and DM the authors solve for the Poisson equation

$$\nabla^2 \Phi_i(\mathbf{x}) = 4\pi G \int d\mathbf{v}^3 f_i(\mathbf{J}), \quad (2)$$

where i can be either stars ($i = \star$) or DM ($i = \text{DM}$). The DF of each component $f_i(\mathbf{J})$ is given by

$$f_i(\mathbf{J}) = f_i \frac{M_i}{(2\pi J_i)^3} \left[1 - \beta \frac{J_{c,i}}{h_i(\mathbf{J})} + \left(\frac{J_{c,i}}{h_i(\mathbf{J})} \right)^2 \right]^{-\frac{\Gamma_i}{2}} \times \left[1 + \left(\frac{J_i}{h_i(\mathbf{J})} \right)^{\eta_i} \right]^{\frac{\Gamma_i}{\eta_i}} \left[1 + \left(\frac{g_i(\mathbf{J})}{J_i} \right)^{\eta_i} \right]^{\frac{\Gamma_i - B_i}{\eta_i}} \times e^{-\left[\frac{g_i(\mathbf{J})}{J_{t,i}} \right]^{\eta_i}}, \quad (3)$$

where

$$h_i(\mathbf{J}) = h_{r,i} J_r + \frac{3 - h_{r,i}}{2} (|J_\phi| + J_z) = h_{r,i} J_r + \frac{3 - h_{r,i}}{2} L \quad (4)$$

and

$$g_i(\mathbf{J}) = g_{r,i} J_r + \frac{3 - g_{r,i}}{2} (|J_\phi| + J_z) = g_{r,i} J_r + \frac{3 - g_{r,i}}{2} L. \quad (5)$$

This DF framework allows for a variety of density profiles, including cored or cuspy density profiles, with different inner and

outer velocity distributions. M_i is the total mass of the target component, $J_{c,i}$, J_i and $J_{t,i}$ are action scales that set the transition between different regimes in the action space (details are provided in Vasiliev 2019 and P24). Γ_i , B_i , and η_i are dimensionless parameters related to the inner and outer slopes of the density profile and the sharpness of the transition between the two. The dimensionless parameters $g_{r,i}$ and $h_{r,i}$, with allowed ranges $0 < g_{r,i} < 3$ and $0 < h_{r,i} < 3$, are related to the model's velocity distributions. The models are spherically symmetric since the DFs (3) depend on the vertical (J_z) and azimuthal (J_ϕ) actions only through the angular momentum modulus $L = J_z + |J_\phi|$.

In Table 2 we provide a convenient summary of the inference on the model's free parameters from P24, alongside the lower and upper bounds of the uniform prior distributions adopted in their Bayesian analysis. Here, it is sufficient to recall that confidence intervals on model parameters and any derived quantity are computed as percentiles from the corresponding marginalized distributions. Specifically, the median model corresponds to the 50th percentile, the 1σ confidence intervals are computed using the 16th and 84th percentiles, while the 3σ confidence intervals as the 0.15th and 99.85th percentiles.

3. Results

In this section, we present and discuss our results, which are based on further analysis of the models of P24. P24 only focused on the central BH properties, but the same models also account for the presence of DM (see Section 2.2), to which we shift our attention here.

3.1. Dark matter density distribution

In Fig. 1 we present an overview on the DM properties of Leo I based on our analysis. The left panel shows the median DM density profile computed from the posterior distribution presented by P24 with the 1σ and 3σ confidence intervals, and, for comparison, the 1σ profiles estimated by R19 and H20. A vertical solid line to the left indicates the upper limit of the BH influence radius¹ estimated by P24, while additional vertical solid lines marking the radius of 150 pc - used for estimates of ρ_{150} - and the effective radius $R_{\text{eff}} = 272$ pc from (McConnachie 2012, see also Table 1). The small panel to the top shows the corresponding logarithmic slope $\gamma \equiv \frac{d \log \rho_{\text{DM}}}{d \log r}$ profiles. The right panel displays the galaxy's enclosed DM mass distribution, and, for reference, we also include the stellar mass profile resulting from our fit. According to our analysis, Leo I is confirmed to be a DM-dominated galaxy, with a dynamical-to-stellar mass ratio (M_{dyn}/M_\star) of $\simeq 6.4$ within R_{eff} , and $\simeq 32.5$ within the stellar truncation radius $r_t = 940$ pc. These ratios correspond to dynamical masses of approximately $2.82^{+0.13}_{-0.13} \times 10^7 M_\odot$ within R_{eff} and $18.70^{+3.79}_{-3.38} \times 10^7 M_\odot$ within r_t (see Table 3).

H20 analyze the DM density distribution of all the classical dSphs using axisymmetric Jeans models. In their approach, both stars and DM are flattened, and they fit the radial distribution of stars alongside the l.o.s. velocity dispersion of stars along the major, minor, and an intermediate axes. The DM halo is represented with a generalized axisymmetric Hernquist profile (Hernquist 1990; Zhao 1996). This model allows for the description of halos with either cuspy central profiles or cored profiles, providing a smooth transition between these configurations. In their

specific analysis, H20 find a general preference for cuspy profiles in most of the dSphs studied, with Leo I being the one with the steepest inner slope (although with considerable uncertainties) with respect to better constrained cusps such as the ones the authors find in Draco or Ursa Minor. R19 employ a non-parametric spherical Jeans approach via the GravSphere (Read & Steger 2017) code to examine inner DM densities across a diverse sample of dwarf galaxies, including both dSphs and dwarf irregulars with varied star formation histories. Their results also indicate a preference for a cuspy profile in Leo I. In addition to the aforementioned studies, in an earlier work, Koch et al. (2007) investigated the DM density profile of Leo I. However, this study did not perform a systematic exploration of the parameter space, and the quality of the available kinematic data prevented the authors from drawing firm conclusions regarding whether a cuspy or cored DM profile is preferred, with both being compatible with the data.

In our analysis, we find that the DM density profile of Leo I asymptotically approaches a median slope of $\gamma = 0$ for small distances (top-left panel of Fig. 1), indicating the presence of a core. This result is in apparent contrast with the cuspy profiles proposed in previous studies. Particularly, when compared to the sample of H20, our results diverge significantly, as their model predicts a slope of $\gamma = -1.35^{+0.32}_{-0.61}$, even steeper than a pure NFW with $\gamma = -1$, indicating a strongly cusped profile. By comparison, our results are more aligned with those of R19. Although R19 report a cuspy profile, their spatial coverage of Leo I is more limited than ours, and within the same radial range, our results are compatible with theirs. As a reference, R19 measure a slope of $\gamma_{150} = -1.15^{+0.33}_{-0.37}$ at $r = 150$ pc, which is consistent within 1σ with our result of $\gamma_{150} = -0.89^{+0.21}_{-0.17}$. To provide a clear representation of the γ_{150} parameter, in the small inset of Fig. 1 we show its posterior. It is worth noting that the core-like nature of our profile, with a slope approaching zero, appears only in the very central regions, at distances smaller than or comparable to the innermost data points used by R19. Also, the top-left panel of Fig. 1 reveals that on the scales of r_{infl} , although the median model suggests a central slope γ close to zero, the distribution of γ exhibits a highly asymmetric tail extending toward $\gamma \simeq -1$, with even smaller values at 3σ . This feature is particularly intriguing, and it arises from the inclusion of a central BH in the models, whose impact on the DM distribution is degenerate with, since it also produces, for $r \rightarrow 0$, a cusp.

We provide a quantitative measure of the core extension in the central regions of the DM halo, defining its core radius, r_c , as the distance from the galaxy center at which the logarithmic slope of the DM density profile is $\gamma = -0.5$. We find $r_c = 72^{+40}_{-32}$ pc, smaller indeed than 150 pc, further supporting the consistency of our results with the findings of R19, and marginally larger than the BH maximum influence radius 20 pc. Additionally, the DM slope at the radius of influence is $\gamma_{r_{\text{infl}}} = -0.16^{+0.12}_{-0.17}$, reinforcing the evidence that only the very innermost regions tend to a cored structure. These quantities are also reported in Table 3 for reference.

The DM density profiles inferred from our models of Leo I consistently indicates a higher normalization across almost all radii when compared to previous profiles in the literature. This discrepancy is especially pronounced at 150 pc, a reference distance used to assess the amount of DM in the centre of dSphs, and thus a scale that is well-constrained by several studies. When compared to H20, who provide a comprehensive estimate of ρ_{150} across all classical dSphs, Leo I emerges as the most DM-dense classical dSph. Although H20 also reported that Leo I has the highest ρ_{150} , our analysis yields a value that is almost twice as

¹ The BH influence radius is estimated as the distance from the galaxy center where the l.o.s. velocity dispersion is equal to the BH circular velocity (Binney & Tremaine 2008).

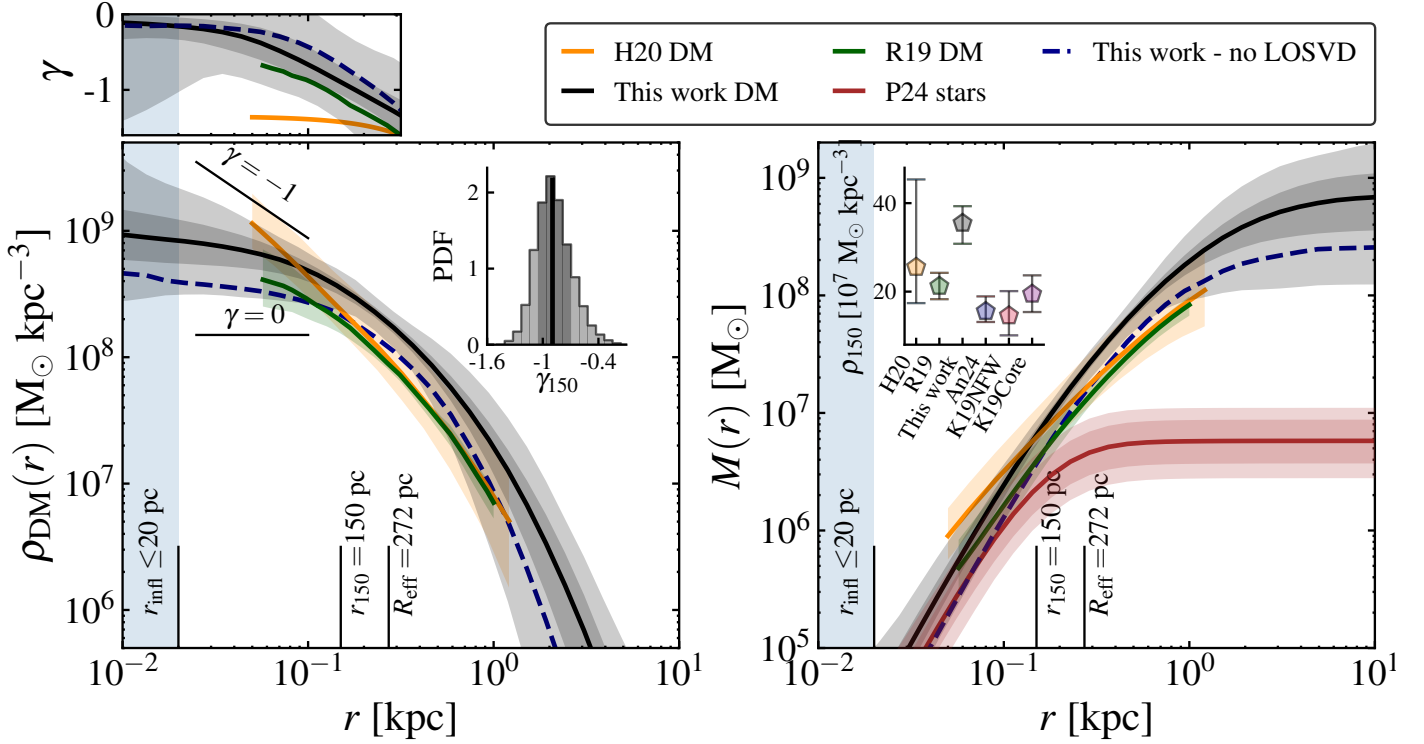


Fig. 1: DM Properties. Left panel: DM density profile from the reference model (black solid line) with 1σ and 3σ confidence intervals (grey bands). The green and orange lines, together with the colored bands, show DM density profiles from [R19](#) and [H20](#), respectively, alongside their 1σ confidence intervals. The blue-dashed line is the median model obtained fitting only the l.o.s. velocity dispersion profile in Section 2.1, with models 2.2. The black vertical line indicates the upper limit on Leo I’s BH influence radius ($r_{\text{infl}} \leq 20$ pc; [P24](#)), while other vertical lines mark 150 pc and the effective radius $R_{\text{eff}} = 272$ pc ([McConnachie 2012](#)). The small panel to the top shows the corresponding logarithmic slope $\gamma \equiv d \ln \rho_{\text{DM}} / d \ln r$. Right panel: same as the left panel, but showing the enclosed DM mass profile. The red line indicates the median stellar mass with 1σ and 3σ uncertainties with a red band. The inset in the left panel shows the posterior distribution on γ_{150} . The inset in the right panel shows a compilation of ρ_{150} (with 1σ errorbars) values from various studies: [R19](#) and [H20](#) (color-coded as in main panels); [Andrade et al. \(2024, An24\)](#) in blue; and [Kaplinghat et al. \(2019, Kap19\)](#) for NFW and cored DM models in red and purple, respectively. Note that [Kaplinghat et al. \(2019\)](#) and [Andrade et al. \(2024\)](#) provide the values of ρ_{150} , but not density profiles.

large, but still consistent within 1σ , reinforcing its status as the densest dSph. The small inset in the right-hand panel of Fig. 1 presents a collection of ρ_{150} from various studies, including those by [H20](#) and [R19](#), along with additional estimates from [Kaplinghat et al. \(2019\)](#) and [Andrade et al. \(2024\)](#), with [Kaplinghat et al. \(2019\)](#) providing two measurements based on different DM models, one assuming a core and the other a cusp. This comparison highlights that the values from [H20](#) has considerably higher uncertainty than all other studies and that our measurement indicates a DM density at 150 pc that is at least twice as high as any previous estimate.

A notable aspect of this discrepancy is that all studies, except for [P24](#), agree with each other within the error bars. Interestingly, these works are consistent despite employing different methods. For instance, [H20](#) use flattened models and compute three separate profiles along the minor, major, and intermediate axes of the galaxy, fitting them with axisymmetric Jeans models. Both [R19](#) and [Kaplinghat et al. \(2019\)](#) fit higher moments of the l.o.s. velocity distribution with spherical Jeans models, while [Andrade et al. \(2024\)](#) adopt DF-based models, as in our work.

The major distinction between the other studies and ours lies in the employed dataset. While all analyses rely on the l.o.s. velocity data from [Mateo et al. \(2008\)](#), [P24](#) incorporates an additional dataset: the central LOSVDs data from [Bustamante-Rosell](#)

[et al. \(2021\)](#). In Fig. 2, we present the velocity dispersion profile derived by [P24](#) (black squares with error bars) alongside the median l.o.s. velocity dispersion model and confidence intervals from [P24](#). For comparison, we also show the velocity dispersion profiles from [H20](#) as yellow points. The profiles from [H20](#) and [P24](#) align closely for $r > 150$ pc, while they diverge within 150 pc, where [P24](#) incorporate the central LOSVDs into the fit. These LOSVDs exhibit velocity dispersions that reach up to 12 km s^{-1} (shown as small black points in Fig. 2), a value higher than the inner profile from [H20](#), which stabilizes around 8 km s^{-1} . The bottom panel of Fig. 2 shows the symmetrized anisotropy parameter $\tilde{\beta}$ defined as ([Read et al. 2006](#))

$$\tilde{\beta} = \frac{\sigma_r^2 - \sigma_\theta^2}{\sigma_r^2 + \sigma_\theta^2}, \quad (6)$$

with σ_r and σ_θ the radial and tangential velocity dispersions, respectively. The parameter $\tilde{\beta}$ is related to the well known anisotropy parameter β ([Binney & Tremaine 2008](#))

$$\tilde{\beta} = \frac{\beta}{2 - \beta}. \quad (7)$$

The advantage of using $\tilde{\beta}$ over β is that $\tilde{\beta}$ is symmetric between -1 and 1 . $\tilde{\beta}$ measures tangential anisotropy when it lies between

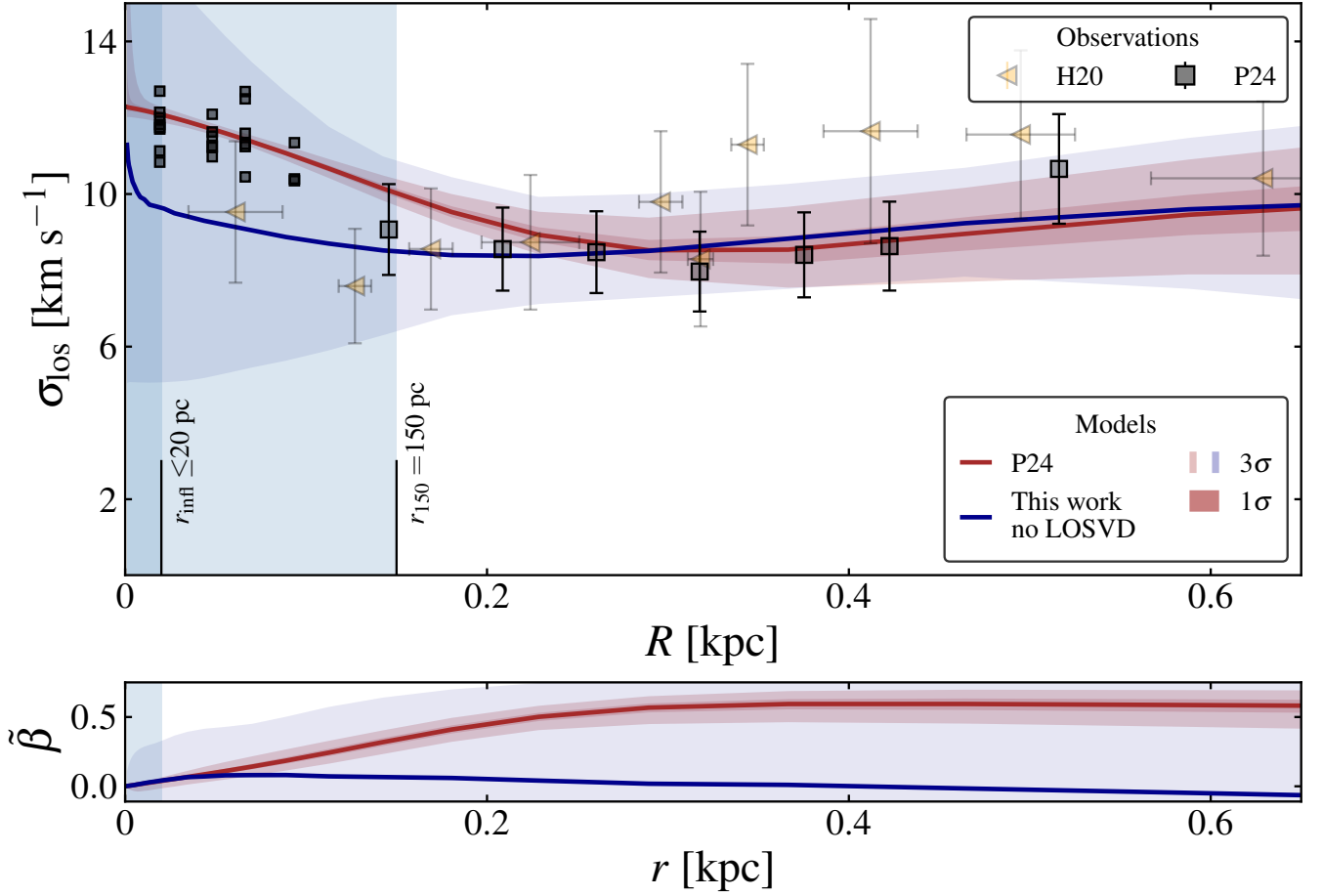


Fig. 2: Kinematic properties of Leo I. Top panel: Median l.o.s. stellar velocity dispersion profile from P24 (solid red line), with shaded regions representing the 1 σ and 3 σ confidence intervals. The blue solid line and the light blue band show, instead, the median l.o.s. velocity dispersion and the 3 σ band obtained fitting the same dataset as P24 except for the central LOSVDs, respectively. Black squares with error bars depict the l.o.s. velocity dispersion from P24 computed with Mateo et al. (2008) data, while the smaller black squares in the inner region show the dispersion of the LOSVDs fitted by P24 (see their figure 2). For comparison, l.o.s. velocity dispersion data from H20 along Leo I’s major axis are shown as yellow triangles with errorbars. The light blue vertical bands mark the regions within Leo I’s BH maximum influence radius ($r_{\text{infl}} \leq 20$ pc) and within 150 pc. Bottom panel: Symmetrized stellar anisotropy parameter profile derived from the median model of P24, including 1 σ and 3 σ confidence intervals. As in the top panel, the red curve and band correspond to the models from P24, while blue curve and band to the models obtained fitting the same dataset as P24 except for the LOSVDs.

−1 and 0 (whereas $\beta < 0$). Both $\tilde{\beta}$ and β are equal to 0 for isotropy, and both $\tilde{\beta}$ and β correspond to radial anisotropy in the range between 0 and 1.

We believe that the inclusion of the additional LOSVD dataset is the primary reason for our higher inferred DM density. To test this hypothesis, we repeated the identical Bayesian model-data comparison performed by P24, but excluding the central LOSVDs. The resulting median DM density, mass and logarithmic slope profiles are reported in Fig. 1. As shown, the DM density profile is fully consistent with those derived in other studies, so does the value of ρ_{150} . In this model, the dynamical mass within R_{eff} and r_t decreases by nearly a factor of two, becoming $1.94^{+0.55}_{-0.38} M_{\odot}$ and $11.54^{+7.48}_{-4.02} M_{\odot}$, respectively. These revised values are in agreement with all previous estimates, including that by Koch et al. (2007). While Koch et al. (2007) provide an estimate of the DM mass within r_t , and we report the total dynamical mass, the system at this radius is effectively DM-dominated, making the two measurements directly comparable.

This behavior can be explained qualitatively as follows, although the interplay between the models’ free parameters is not necessarily straightforward. The central LOSVDs, whose dispersions are particularly high when compared to the outer l.o.s. velocity dispersion profile, increase the amount of mass required in these regions and. This leads to an overall increase of DM density for a fixed anisotropy. At the same time, to fit the outer l.o.s. velocity dispersion profile, a strong radial anisotropy in the outer regions is favored (see the bottom panel of Fig. 2). This is because radial anisotropy results into an increase of the velocity dispersion along the radial component, which in turn decreases the l.o.s. velocity dispersion profile in outskirts (Pascale et al. 2019).

Residual differences between our inferred DM density profiles and those reported in previous studies may be attributed to the use of slightly different surface brightness or stellar density profiles by various authors. As discussed in Section 2.1, the surface brightness profiles commonly adopted in the modeling of dSphs are derived from ground-based observations, which inevitably carry systematic biases and limitations. Moreover, un-

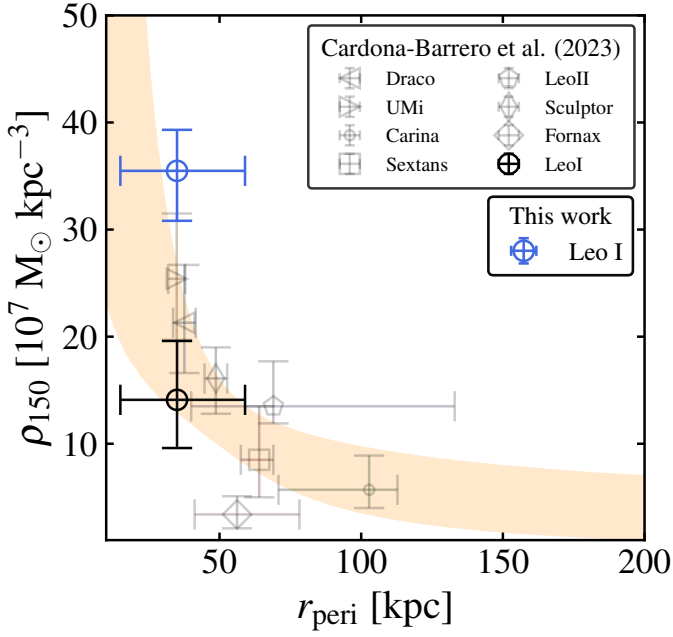


Fig. 3: $r_{\text{peri}} - \rho_{150}$ anticorrelation for the eight classical dSphs from Cardona-Barrero et al. (2023). Central ρ_{150} densities are taken from Kaplinghat et al. (2019), while pericentric distances are from Battaglia et al. (2022). The orange band represents the fit to the grey and black points as derived by Cardona-Barrero et al. (2023). The blue point corresponds to the measurement for Leo I, with ρ_{150} derived in this work.

like other works where these profiles serve as fixed inputs to the models, in our approach they are fitted simultaneously with the kinematic data, properly accounting for observational uncertainties, which may also contribute to these discrepancies.

Regarding the large 1σ confidence levels in the mass and density (and, thus, ρ_{150}) distributions reported by H20, we believe that these arise from their use of flattened models, which allow for marginalization over the flattening of the DM halo. This approach likely increases the uncertainty in the inferred density estimates, resulting in the broader error ranges measured in their study.

3.2. Central density versus pericentric distance anticorrelation

The advent of Gaia Data Release 2 (GDR2) has provided precise proper motion measurements of the bulk velocity of dSphs, significantly improving the reconstruction of their orbits within the Milky Way potential. This led several studies to identify a potential anticorrelation between the pericentric distance, r_{peri} , and the central DM density, ρ_{150} , of the classical dSphs (Kaplinghat et al. 2019; Cardona-Barrero et al. 2023). Such a trend implies that dSphs that pass closer to the Galactic center tend to have higher central DM density. However, the existence of this anticorrelation remains highly debated, and its underlying physical origin is still uncertain. A few mechanisms have been proposed to explain it.

For instance, the so-called "survivor bias" model (H20) posits that low-density dSphs with small pericentric distances have been disrupted by tidal interactions, leaving behind only the densest systems. However, this scenario fails to explain why galaxies with high ρ_{150} and large r_{peri} are absent. Instead, some

Table 3: DM and stellar parameters computed from the posterior of P24.

Parameter	1σ
$M_{\text{dyn}}/M_{\star}(R_{\text{eff}})$	$6.4^{+3.6}_{-2.2}$
$M_{\text{dyn}}/M_{\star}(r_t)$	$32.5^{+18.2}_{-11.0}$
$M_{\text{dyn}}(R_{\text{eff}}) [10^7 M_{\odot}]$	$2.82^{+0.13}_{-0.13}$
$M_{\text{dyn}}(r_t) [10^7 M_{\odot}]$	$18.70^{+3.79}_{-3.38}$
$\rho_{150} [10^7 M_{\odot} \text{ kpc}^{-3}]$	$35.5^{+3.8}_{-4.7}$
$r_c [\text{pc}]$	72^{+40}_{-32}
$\gamma_{r_{\text{infl}}}$	$-0.16^{+0.12}_{-0.17}$
γ_{150}	$-0.89^{+0.21}_{-0.17}$
$\log D(0.5^\circ) [\text{GeV cm}^{-2}]$	$17.94^{+0.17}_{-0.25}$
$\log J(0.5^\circ) [\text{GeV}^2 \text{ cm}^{-5}]$	$18.13^{+0.17}_{-0.18}$

Notes. From top to bottom: dynamical-to-stellar mass ratio within the stellar effective radius, $M_{\text{dyn}}/M_{\star}(R_{\text{eff}})$, and within the stellar truncation radius, $M_{\text{dyn}}/M_{\star}(r_t)$; dynamical mass within the stellar effective radius, $M_{\text{dyn}}(R_{\text{eff}})$, and within the stellar truncation radius $M_{\text{dyn}}(r_t)$; DM density at 150 pc, ρ_{150} ; core radius of DM halo, r_c , logslope γ measured at the BH's maximum influence radius, $\gamma_{r_{\text{infl}}}$, and at 150 pc, γ_{150} ; DM decay D -factor within 0.5° , $\log D(0.5^\circ)$, and DM annihilation J -factor within 0.5° , $\log J(0.5^\circ)$.

authors suggest that the anticorrelation could naturally arise in alternative DM scenarios, due to intrinsic and different properties of DM in non-standard scenarios. For instance, the anticorrelation might arise as a consequence of tidal-stripping-driven gravothermal core collapse of the satellite dwarf halos (Correa et al. 2015) in the context of self-interacting DM (SIDM). Others argue that the anticorrelation is merely an artifact of incompleteness or biased parameter estimates, rather than a genuine physical relationship. The anticorrelation is particularly controversial, as no similar trend has been observed in the population of ultrafaint dwarf galaxies, also satellites of the Milky Way.

In a recent work, Cardona-Barrero et al. (2023) gathered different sets of central DM densities and pericentric distances from various studies (Kaplinghat et al. 2019; Hayashi et al. 2020; Battaglia et al. 2022), and explored multiple combinations of these datasets to assess the statistical occurrence of the proposed anticorrelation. Their analysis also incorporates r_{peri} estimates that account for the time-dependent Milky Way potential, including the influence of the Large Magellanic Cloud's infall, in order to marginalize and examine potential biases arising from the use of specific datasets and different assumptions. The results indicate that the anticorrelation is statistically significant in only 12% of the analyzed dataset combinations, suggesting that evidence for this relationship is, apparently, weak and highly sensitive to the choice of datasets.

In Fig. 3, we show an illustrative example of the 24 $\rho_{150}-r_{\text{peri}}$ combinations explored by Cardona-Barrero et al. (2023), along with their fitted anticorrelation (the "linear" fit proposed by the authors is in log-log space). While this is not the case where the anticorrelation is intrinsically the most significant, it remains detectable at the 1σ level according to Cardona-Barrero et al. (2023). Our revised ρ_{150} estimate (blue point) further strengthens this trend, shifting the innermost data point upward. This is a particularly striking aspect, as it significantly enhances the

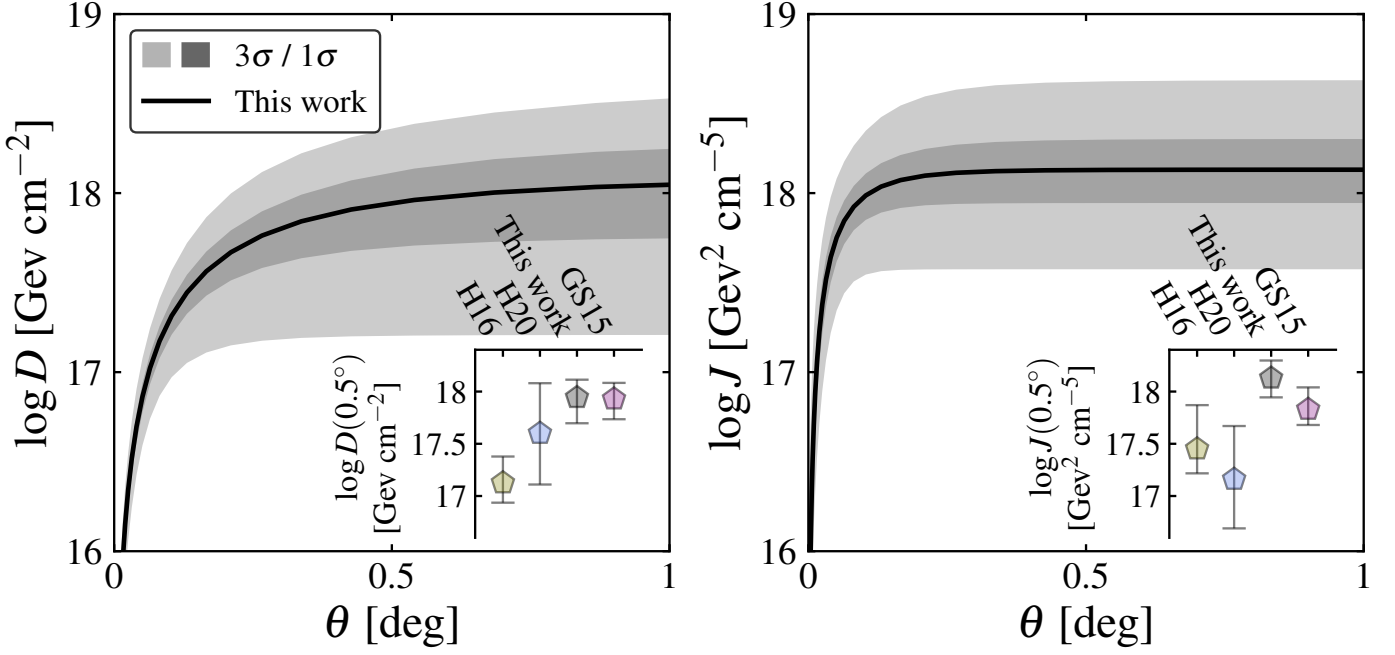


Fig. 4: Left panel: DM decay D -factor computed from the reference model of P24 (black solid line) together with the 1σ and 3σ bands. Right panel: same as the left panel but showing the model’s J -factor profile. The small insets in the bottom panel show the models D and J factors at an aperture of 0.5° compared to values from the literature: Hayashi et al. (2020, H16) in yellow, Hayashi et al. (2020) and Geringer-Sameth et al. (2015, GS15) in purple.

anticorrelation, making it much more pronounced. This adjustment may increase the statistical significance of the anticorrelation in dataset combinations that previously showed weak or no evidence for it.

3.3. J and D factors

The J - and D - factors are key quantities for indirect DM detection experiments. These experiments focus on searching for gamma-ray emission resulting from DM annihilation (J -factor) and decay (D -factor) within systems with possibly a large amount of DM (e.g. Zeldovich et al. 1980; Turner et al. 1984). In this respect, dSphs are of particular interest since they are DM-dominated, but also they lack other sources in the gamma-ray band, and, additionally, they are relatively close to Earth. To date, no significant gamma-ray excess has been detected from dSphs, and all constraints on DM particle properties are based on non-detections. These non-detections have been used to place upper limits on the annihilation cross-sections and particle masses of DM candidates, with some studies ruling out certain classes of particles as viable explanations for the observed data (Ackermann et al. 2015; Geringer-Sameth et al. 2015; Hoof et al. 2020; Di Mauro et al. 2022; Crnogorčević & Linden 2024). Despite the absence of direct signals, these galaxies remain prime targets for future DM searches.

The J factor quantifies the probability of detecting a gamma-ray signal resulting from the annihilation of DM particles. Similarly, the D factor relates to the probability of gamma-ray emission due to the decay of DM particles. These factors are defined as (Evans et al. 2016)

$$J(\theta) = \frac{2\pi}{d^2} \int_{-\infty}^{+\infty} dz \int_0^{\theta d} \rho_{\text{DM}}^2(R, z) R dR, \quad (8)$$

and

$$D(\theta) = \frac{2\pi}{d^2} \int_{-\infty}^{+\infty} dz \int_0^{\theta d} \rho_{\text{DM}}(R, z) R dR, \quad (9)$$

where d is the distance of the galaxy, while θ is the angular distance measured from the center of the galaxy, z is the l.o.s. while R is the distance from the center of the galaxy on the plane of the sky. It is essential to note that the J and D factors are determined by two main factors: the DM density profile of the galaxy and its distance from the Earth. Leo I is particularly interesting as it is the most DM-dense dSphs, yet it is also the most distant, leading to some trade-offs in terms of its DM signature.

Fig. 4 shows the profiles of the J and D factors for Leo I as a function of the angular distance from the galaxy center, computed based on the posterior distributions from P24. Typically, J and D factors are calculated within a region of 0.5° , which corresponds to the resolution of the Fermi LAT telescope. In Fig. 4, the small insets also provide comparisons with values from previous studies in the literature. While the new estimate of the D is generally consistent within the error bars with previous estimates, the values of the J factor differ significantly. Our new estimate of the J factor is more than one sigma higher than the values reported by Hayashi et al. (2016, 2020) and is marginally compatible with Geringer-Sameth et al. (2015). This discrepancy in the J factor is likely due to the quadratic dependence on the DM density profile, which may accentuate differences in the J factor for a given distance from the galaxy’s center more than in the D factor.

Compared to other dwarf galaxies, our new estimate of the J factor places Leo I as a more favorable target than previously suggested. However, it is still not among the most promising dSphs for DM searches. Even though recent studies show that galaxies such as Fornax (Pascale et al. 2019) and Sculptor (Arroyo-Polonio et al. in prep.) exhibit systematically higher J

and D factors than previously estimated (see also Nipoti et al. 2024), other galaxies, such as Draco and Ursa Minor, remain among the most favorable targets for DM detection (see, for instance, Geringer-Sameth et al. 2015).

4. Conclusions

This study provides a revised characterization of the DM properties of the dSph Leo I. Building on the results of P24, we have conducted an in-depth analysis of the DM distribution in the galaxy. The models here presented leverage state-of-the-art dynamical models based on $f(J)$ DFs and fit the central galaxy LOSVDs from Bustamante-Rosell et al. (2021), as well as photometric and outer spectroscopic measurements from Bustamante-Rosell et al. (2021) and Mateo et al. (2008). While P24 primarily investigated the presence of a possible IMBH in Leo I, this study shifts the attention to the DM properties inferred from the same models. According to our new estimate, Leo I is the classical dSph known in the MW with the highest DM density. As a reference, we provide a central DM density of $\rho_{150} = 35.5^{+3.8}_{-4.7} \times 10^7 M_\odot \text{ kpc}^{-3}$ at 150 pc from the galaxy center.

This new estimate has important implications for the anti-correlation between central DM density and the pericentric distance of MW satellites, whose physical origin remains an open question. For instance, DM-only simulations suggest a strong anti-correlation (Hayashi et al. 2016), whereas hydrodynamical simulations incorporating baryonic effects indicate that the MW's disk potential can significantly alter satellite densities, leading to lower densities in satellites with smaller pericenters (Robles et al. 2019). While Cardona-Barrero et al. (2023) recently demonstrated that the existence and strength of this anti-correlation depend on the used dataset - with a clear signal emerging only in certain cases - our revised and larger estimate of Leo I's DM density could strengthen the observed trend.

Our results on the central DM density of Leo I are also relevant to SIDM models. Correa (2021), exploring models of SIDM with a velocity-dependent cross section, finds that Leo I favours a SIDM cross section larger than found for other dSphs with similar velocity dispersion. Using our estimate of ρ_{150} for Leo I, which is higher than that of Kaplinghat et al. (2019), used by Correa (2021), this conclusion is strengthened, because more efficient gravothermal collapse is required to produce a higher central DM density. Ebisu et al. (2022) show that SIDM models with velocity-independent cross section are hard to reconcile with the observed ρ_{150} - r_{peri} anticorrelation, because they predict dwarf galaxies with lower ρ_{150} than observed in classical dSphs, with Leo I being one of the galaxies with the strongest discrepancy: this discrepancy worsens if the central DM density of Leo I is as high as estimated in our work.

We also explored the structure of the DM distribution in the context of the core-cusp problem. Our results indicate that Leo I's internal kinematics is compatible with the presence of a central DM core. We measure a core size (the distance from the galaxy center where the logslope $\gamma = -0.5$) of $r_c = 72^{+40}_{-32}$ pc, larger than the maximum sphere of influence of a putative IMBH ($r_{\text{infl}} = 20$ pc). Here, we measure a logarithmic slope $\gamma_{r_{\text{infl}}} = -0.16^{+0.12}_{-0.17}$. At larger radii, which correspond to the innermost regions covered by data in several studies from the literature, the DM density profile exhibits a mild cusp, with a logarithmic slope of $\gamma_{150} = -0.89^{+0.21}_{-0.17}$ at 150 pc.

Finally, we provide new estimates of the J and D factors for Leo I, obtaining $\log D(0.5^\circ) [\text{GeV cm}^{-2}] = 17.94^{+0.17}_{-0.25}$ and $\log J(0.5^\circ) [\text{GeV}^2 \text{ cm}^{-5}] = 18.13^{+0.17}_{-0.18}$. Although these values are

higher than some previous estimates, they remain within the range of literature values for Leo I. Thus, despite its status as a highly DM-dominated system, Leo I does not emerge as one of the most promising dSph targets for indirect DM detection via gamma-ray emission.

A key difficulty in determining the surface brightness profiles of dSph galaxies lies in the use of wide-field ground-based imaging, where issues such as crowding, background subtraction, and the trade-off between field of view and spatial resolution, hence uniform coverage of the target, become significant. As a result, dynamical models relying on these profiles inherently carry a level of uncertainty associated with how the profiles themselves are constructed. Euclid will substantially mitigate these limitations: its imager combines a 0.57 deg field of view with spatial resolution (FWHM) $\simeq 0.14$ arcsec in VIS (I band) and $\simeq 0.45$ arcsec in NISP (Y, J, H bands; Cuillandre et al. 2025), and a diffraction-limited PSF, enabling uniform, background-limited photometry down to I band magnitude $\simeq 30$ mag arcsec $^{-2}$ (Hunt et al. 2025). For Leo I, this translates into: (i) continuous coverage of the target beyond 40 arcsec in a single pointing; (ii) lower crowding and thus deeper stellar photometry; and (iii) self-consistent photometric calibration on a single detector, which minimizes completeness variations. Euclid is therefore expected to revolutionize the field of dynamical modeling by providing unprecedentedly high-quality data for Leo I, as well as for dSph galaxies and, generally, low-surface-brightness galaxies.

Acknowledgements. We are grateful to the referee, Prof. G. Gilmore, for the useful comments and feedback that helped improve the quality of the paper. We also thank Dr. Francesca Annibali for her constructive feedback and suggestions. This paper is supported by the Italian Research Center on High Performance Computing Big Data and Quantum Computing (ICSC), project funded by European Union - NextGenerationEU - and National Recovery and Resilience Plan (NRRP) - Mission 4 Component 2 within the activities of Spoke 3 (Astrophysics and Cosmos Observations). The research activities described in this paper have been co-funded by the European Union - NextGenerationEU within PRIN 2022 project n.20229YBSAN - Globular clusters in cosmological simulations and in lensed fields: from their birth to the present epoch.

References

- Ackermann, M., Albert, A., Anderson, B., et al. 2015, *Phys. Rev. Lett.*, 115, 231301
- Amorisco, N. C. & Evans, N. W. 2011, *MNRAS*, 411, 2118
- Andrade, K. E., Kaplinghat, M., & Valli, M. 2024, *MNRAS*, 532, 4157
- Arroyo-Polonio, J., Pascale, R., Battaglia, G., Guillaume, F. T., & C., N. in prep.
- Battaglia, G. & Nipoti, C. 2022, *Nature Astronomy*, 6, 659
- Battaglia, G., Taibi, S., Thomas, G. F., & Fritz, T. K. 2022, *A&A*, 657, A54
- Bellazzini, M., Gennari, N., Ferraro, F. R., & Sollima, A. 2004, *MNRAS*, 354, 708
- Binney, J. 2014, *MNRAS*, 440, 787
- Binney, J. & Tremaine, S. 2008, *Galactic Dynamics: Second Edition* (Princeton University Press)
- Boddy, K. K., Kumar, J., Pace, A. B., Runburg, J., & Strigari, L. E. 2020, *Phys. Rev. D*, 102, 023029
- Bonnivard, V., Combet, C., Daniel, M., et al. 2015, *MNRAS*, 453, 849
- Breddels, M. A. & Helmi, A. 2013, *A&A*, 558, A35
- Bullock, J. S. & Boylan-Kolchin, M. 2017, *ARA&A*, 55, 343
- Bustamante-Rosell, M. J., Noyola, E., Gebhardt, K., et al. 2021, *ApJ*, 921, 107
- Cardona-Barrero, S., Battaglia, G., Nipoti, C., & Di Cintio, A. 2023, *MNRAS*, 522, 3058
- Cole, D. R. & Binney, J. 2017, *MNRAS*, 465, 798
- Correa, C. A. 2021, *MNRAS*, 503, 920
- Correa, C. A., Wyithe, J. S. B., Schaye, J., & Duffy, A. R. 2015, *MNRAS*, 452, 1217
- Crnogorčević, M. & Linden, T. 2024, *Phys. Rev. D*, 109, 083018
- Cuillandre, J. C., Bertin, E., Bolzonella, M., et al. 2025, *A&A*, 697, A6
- de Blok, W. J. G. 2010, *Advances in Astronomy*, 2010, 789293
- Di Mauro, M., Stref, M., & Calore, F. 2022, *Phys. Rev. D*, 106, 123032
- Ebisu, T., Ishiyama, T., & Hayashi, K. 2022, *Phys. Rev. D*, 105, 023016

- Evans, N. W., Sanders, J. L., & Geringer-Sameth, A. 2016, *Phys. Rev. D*, 93, 103512
- Fritz, T. K., Battaglia, G., Pawlowski, M. S., et al. 2018, *A&A*, 619, A103
- Gaia Collaboration, Helmi, A., van Leeuwen, F., et al. 2018, *A&A*, 616, A12
- Geringer-Sameth, A., Koushiappas, S. M., & Walker, M. 2015, *ApJ*, 801, 74
- Gilmore, G., Wilkinson, M. I., Wyse, R. F. G., et al. 2007, *ApJ*, 663, 948
- Governato, F., Weisz, D., Pontzen, A., et al. 2015, *MNRAS*, 448, 792
- Governato, F., Zolotov, A., Pontzen, A., et al. 2012, *MNRAS*, 422, 1231
- Hayashi, K., Chiba, M., & Ishiyama, T. 2020, *ApJ*, 904, 45
- Hayashi, K., Ichikawa, K., Matsumoto, S., et al. 2016, *MNRAS*, 461, 2914
- Held, E. V., Gullieuszik, M., Rizzi, L., et al. 2010, *MNRAS*, 404, 1475
- Hernquist, L. 1990, *ApJ*, 356, 359
- Hoof, S., Geringer-Sameth, A., & Trotta, R. 2020, *J. Cosmology Astropart. Phys.*, 2020, 012
- Hui, L., Ostriker, J. P., Tremaine, S., & Witten, E. 2017, *Phys. Rev. D*, 95, 043541
- Hunt, L. K., Annibali, F., Cuillandre, J. C., et al. 2025, *A&A*, 697, A9
- Irwin, M., & Hatzidimitriou, D. 1995, *MNRAS*, 277, 1354
- Kaplinghat, M., Valli, M., & Yu, H.-B. 2019, *MNRAS*, 490, 231
- Koch, A., Wilkinson, M. I., Kleyna, J. T., et al. 2007, *ApJ*, 657, 241
- Lacey, C. & Cole, S. 1993, *MNRAS*, 262, 627
- Lacey, C. & Cole, S. 1994, *MNRAS*, 271, 676
- Li, S., Liang, Y.-F., & Fan, Y.-Z. 2021, *Phys. Rev. D*, 104, 083037
- Marzke, R. O., da Costa, L. N., Pellegrini, P. S., Willmer, C. N. A., & Geller, M. J. 1998, *ApJ*, 503, 617
- Mateo, M., Olszewski, E. W., & Walker, M. G. 2008, *ApJ*, 675, 201
- McConnachie, A. W. 2012, *AJ*, 144, 4
- Méndez, B., Davis, M., Moustakas, J., et al. 2002, *AJ*, 124, 213
- Muñoz, R. R., Côté, P., Santana, F. A., et al. 2018, *ApJ*, 860, 66
- Nipoti, C. & Binney, J. 2015, *MNRAS*, 446, 1820
- Nipoti, C., Pascale, R., & Arroyo-Polonio, J. M. 2024, *arXiv e-prints*, arXiv:2411.05084
- Pacucci, F., Ni, Y., & Loeb, A. 2023, *ApJ*, 956, L37
- Pascale, R., Binney, J., Nipoti, C., & Posti, L. 2019, *MNRAS*, 488, 2423
- Pascale, R., Nipoti, C., Calura, F., & Della Croce, A. 2024, *A&A*, 684, L19
- Pascale, R., Posti, L., Nipoti, C., & Binney, J. 2018, *MNRAS*, 480, 927
- Read, J. I. & Gilmore, G. 2005, *MNRAS*, 356, 107
- Read, J. I. & Steger, P. 2017, *MNRAS*, 471, 4541
- Read, J. I., Walker, M. G., & Steger, P. 2019, *MNRAS*, 484, 1401
- Read, J. I., Wilkinson, M. I., Evans, N. W., Gilmore, G., & Kleyna, J. T. 2006, *MNRAS*, 366, 429
- Robles, V. H., Kelley, T., Bullock, J. S., & Kaplinghat, M. 2019, *MNRAS*, 490, 2117
- Ruiz-Lara, T., Gallart, C., Monelli, M., et al. 2021, *MNRAS*, 501, 3962
- Sales, L. V., Wetzel, A., & Fattahi, A. 2022, *Nature Astronomy*, 6, 897
- Sohn, S. T., Besla, G., van der Marel, R. P., et al. 2013, *ApJ*, 768, 139
- Strigari, L. E., Bullock, J. S., Kaplinghat, M., et al. 2008, *Nature*, 454, 1096
- Strigari, L. E., Frenk, C. S., & White, S. D. M. 2017, *ApJ*, 838, 123
- Turner, M. S., Steigman, G., & Krauss, L. M. 1984, *Phys. Rev. Lett.*, 52, 2090
- Vasiliev, E. 2019, *MNRAS*, 482, 1525
- Walker, M. G., Mateo, M., Olszewski, E. W., et al. 2009, *ApJ*, 704, 1274
- Zeldovich, Y. B., Klypin, A., Khlopov, M. Y., & Chechetkin, V. M. 1980, *Soviet Journal of Nuclear Physics*, 31, 664
- Zhao, H. 1996, *MNRAS*, 278, 488